fractal and fractional

MDPI

Article

Effectiveness of Radiation on Magneto-Combined Convective Boundary Layer Flow in Polar Nanofluid around a Spherical Shape

Mohammed Z. Swalmeh [1,2], Feras Shatat [3], Firas A. Alwawi [4], Mohd Asrul Hery Ibrahim [2], Ibrahim Mohammed Sulaiman [5], Nusayba Yaseen [1] and Mohammad F. M. Naser [6,*]

1 Faculty of Arts and Sciences, Aqaba University of Technology, Aqaba 77110, Jordan; msawalmeh@aut.edu.jo (M.Z.S.); nyaseen@aut.edu.jo (N.Y.)
2 Faculty of Entrepreneurship and Business, Universiti Malaysia Kelantan, Kota Bharu 16100, Kelantan, Malaysia; hery.i@umk.edu.my
3 Faculty of Engineering, Liwa College of Technology, Abu Dabi 41009, United Arab Emirates; feras.shatat@ect.ac.ae
4 Department of Mathematics, College of Sciences and Humanities in Al-Kharj, Prince Sattam bin Abdulaziz University, Al-Kharj 11942, Saudi Arabia; f.alwawi@psau.edu.sa
5 Institute of Strategic Industrial Decision Modelling (ISIDM), School of Quantitative Sciences, Universiti Utara Malaysia, Sintok 06010, Kedah, Malaysia; i.mohammed.sulaiman@uum.edu.my
6 Faculty of Engineering Technology, Al-Balqa Applied University, Amman 11134, Jordan
* Correspondence: mohmmad.naser@bau.edu.jo

Abstract: Many physical aspects emerging from the local structure and micromotions of liquid particles can be studied by utilizing the governing model of micropolar liquid. It has the ability to explain the behavior of a wide range of real fluids, including polymeric solutions, liquid crystals, lubricants, and animal blood. This earned it a major role in the treatment of many industrial and engineering applications. Radiative heat transmission induced by a combined convection flow of micropolar fluid over a solid sphere, and its enhancement via nanoparticle oxides, are investigated in this study. An applied magnetic field and a constant wall temperature are also considered. The Tiwari–Das model is used to construct the mathematical model. An approximate numerical solution is included using the Keller box method, in which its numerical calculations are performed via MATLAB software, to obtain numerical results and graphic outputs reflecting the effects of critical parameters on the physical quantities associated with heat transfer. The investigation results point out that a weakness in the intensity of the magnetic field, or an increment in the nanoparticle volume fraction, causes an increment in velocity. Raising the radiation parameter promotes energy transport, angular velocity, and velocity.

Keywords: heat transfer; convection boundary layer flow; nanofluid; solid sphere; magnetic field; radiation effect

Citation: Swalmeh, M.Z.; Shatat, F.; Alwawi, F.A.; Ibrahim, M.A.H.; Sulaiman, I.M.; Yaseen, N.; Naser, M.F.M. Effectiveness of Radiation on Magneto-Combined Convective Boundary Layer Flow in Polar Nanofluid around a Spherical Shape. *Fractal Fract.* **2022**, *6*, 383. https://doi.org/10.3390/fractalfract6070383

Academic Editors: Lanre Akinyemi, Mostafa M. A. Khater, Mehmet Senol and Hadi Rezazadeh

Received: 26 May 2022
Accepted: 29 June 2022
Published: 6 July 2022

1. Introduction

Researchers lately focused on the phenomena of heat transfer enhancement based on the utilization of nanoparticles, revealing that the viscosity of the base fluid and the effectiveness of the thermal conductivity can be improved by the employment of metallic and non-metallic nanoparticles [1–5]. These progressive features made the topic of nanosolids a new technology of interest, which is reflected in the application in various functions of manufacturing procedures, mainly groundwater pollution, heat exchangers, thermal engineering, enhanced oil recovery, cooling phenomena, geothermal systems, magnetic cell separation, crude oil extraction, energy production, and nuclear waste storage, etc. [6–11]. In this regard, many studies were conducted that simulate the extent of the improvement

in energy transport caused by these nanoparticles, and the most important factors influencing it. Khanafer et al. [12] investigate the enhancement of energy transmission utilizing nanofluids, while taking solid particle dispersion into consideration. Buongiorno [13] reports the influence of Brownian motion and thermophoresis on energy transport. Tiwari and Das [14] elucidate the critical effect of the volume fraction of nanosolids in the heat transport process. Ho et al. [15] provide an intriguing numerical examination of the influences due to uncertainties in viscosity and thermal conductivity on free convection. Nield and Kuznetsov [16] extend the Cheng–Minkowycz problem to the case of nanofluids, with the assistance of the Buongiorno model. Then, Kuznetsov and Nield [17] present a study in which the previous model is improved to include the case in which the size of the particles is passively controlled. Das et al. [18] model the entropy generation for magnetized nanoliquid flowing around an accelerating stretching sheet. Shahid et al. [19] study MHD nanoliquid flow, including gyrotactic microorganisms spreading on a stretching surface. Alwawi et al. [20] investigate the MHD mixed and combined convection of sodium alginate and carboxymethyl cellulose-water based Casson nanofluids flowing over spheres. More noteworthy reports are found in these refs. [21–24].

Lately, micropolar flow was an important subject of research because of its important role in many engineering and industrial applications problems, such as cervical flows, thrust-bearing technologies, radial diffusion paint rheology, and clean and contaminated engine lubricants, among others [25]. The dynamics of micropolar fluid was first mentioned in the theory of Eringen et al. [26,27], which considers the effect of local rotary inertia and couple stresses associated with practical micro-rotation. The micropolar fluids are popular non-Newtonian fluids with microstructures that consist of rigid particles and colloidal fluid elements, and are used in making apparatuses for chemical procedures, as well as various heat exchangers [28]. This, and many other applications, including, but not limited to, polymer preparing, and wire and fiber coating of the fluids, require utter understanding of the motion procedure. However, studies on micropolar fluids received a lot of attention recently, due to their vast applications. Khader and Sharma [29] examine the effect of a non-uniform heat source and thermal radiation on unsteady MHD micropolar fluid flow over a shirking/stretching sheet. Kumbinarasaiah and Raghunatha [30] investigate the two-dimensional flow of a rotating micropolar fluid in a porous channel, using the Laguerre wavelet exact Parseval frame method (LWPM). Bhat and Katagi [31] use the Keller box method to examine the steady and two-dimensional micropolar fluid flow between a porous and nonporous disk. Bilal et al. [32] examine the effect of thermal radiation of micropolar fluid across a permeable stretching surface. Abas et al. [33] study magnetohydrodynamic (MHD) dissipative micropolar fluid flow over a stretching sheet, with heat generation and slip effects. Mahabaleshwar et al. [33] examine the flow of an inclined MHD micropolar fluid in the presence of mass transpiration and thermal radiation. More recent studies on this subject are referred to in [34–36].

Magnetohydrodynamic (MHD) has the ability to optimize the transfer of heat from electrically conductive fluid, manipulate the fluid flow, and control separation flow. Therefore, in terms of industrial and engineering applications, the MHD flow is an important research topic that needs to be considered. Currently, more considerable attention was given to the study of MHD mixed convention flow around geometric surfaces [37]. For instance, Ibrahim and Zemedu [38] examine the MHD mixed convection boundary layer over a non-isothermal sphere with Soret and magnetic field effects. On the other hand, a study on the magnetic micropolar nanofluid oblique flow is presented by Tabassum et al. [39], in the presence of mixed convection. Moreover, Mkhatshwa et al. [40] consider the hall effect, chemical reaction, thermo-diffusion, and diffusion–thermal effects to investigate the MHD mixed conventional flow around a vertical cylinder, and Rahman et al. [41] investigate the MHD mixed convection over a horizontal circular cylinder that can conduct heat, and is placed at the center of a rectangular cavity. More information on this topic is found in [42–45]. On the other hand, thermal radiation effects recently received significant attention in the field of fluid dynamics. Physically, it is formed

by the presence of surface gravity waves, which are propagated along the mean of the boundary layer flow. In addition, thermal radiation plays a wide role in the numerical solution investigations for heat transfer and temperature distributions in the existence of the boundary layer flow. Moreover, Mansour and Gorla [46] and Mohammadein and El-Amin [47] study the influence of thermal radiation on convection boundary layer flow with non-Newtonian fluids over a non-isothermal wedge and horizontal plate, respectively. Furthermore, [48–52] consider the radiation heat and mass transfer in mixed convection boundary layer flow on a solid sphere. Additionally, the mixed convection in micropolar fluid and radiation characteristics gained more attention in the literature, e.g., [52–55].

Keeping in mind the above numerical studies of the convection boundary layer flow, the existing work is concerned with mixed convection heat transfer characteristics for thermal radiation in micropolar nanofluid flowing under a magnetic field. To this end, a model was constructed for analyzing the nanoparticles, comprising of alumina and copper oxide, suspended in base fluids, considering the solid sphere geometry. In addition, the famous Tiwari–Das model was also employed in this study. After transforming the dimensional equations into partial differential equations, we then utilized the Keller box method to solve the resultant equations. The results obtained were compared with the previous literature to show their good agreement.

2. Basic Equations

Mixed convection with a uniform free stream U_∞, on a solid sphere of radius a with constant wall temperature T_w, in the presence of micropolar nanofluid with magnetic field strength B_0, was investigated numerically in this paper. Two types of metals, namely, alumina oxide and copper oxide, were suspended in two different types of fluids, namely, water and methanol. Figure 1 shows the physical coordinate model system, the free stream temperature T_∞, and $\hat{\aleph} - \hat{\gamma}$ are the perpendicular coordinates on the surface of the solid sphere. A heated and cooled sphere ($T_w > T_\infty$ and $T_w < T_\infty$, respectively) were also taken into account.

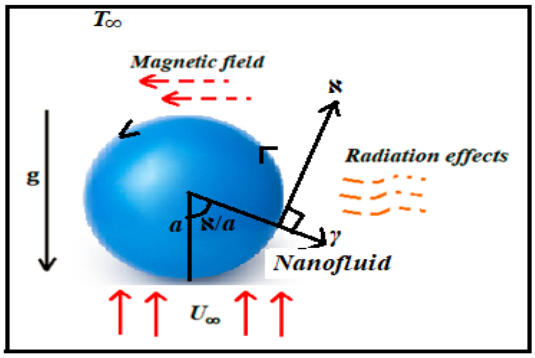

Figure 1. Physical model and coordinate system.

Under Boussinesq and boundary layer approximations, as well as utilizing the Tiwari–Das nanofluid model, considering magnetic and thermal radiation effects, the continuity, momentum, and energy micropolar equations are [14,47,54]:

$$\hat{\nabla}.\hat{V} = 0, \tag{1}$$

$$\left(\hat{V}.\hat{\nabla}\right)\hat{V} = -\frac{1}{\rho_{nf}}\hat{\nabla}\hat{P} + \left(\frac{\mu_{nf}+\kappa}{\rho_{nf}}\right)\hat{\nabla}^2\hat{V} + \frac{\kappa}{\rho_{nf}}\left(\frac{\partial\hat{N}}{\partial\hat{\gamma}} - \frac{\partial\hat{N}}{\partial\hat{\aleph}}\right) + \frac{\left(\chi\rho_s\beta_s+(1-\chi)\rho_f\beta_f\right)}{\rho_{nf}}\hat{g}(T - T_\infty) - \frac{\sigma_{nf}}{\rho_{nf}}B_0^2\hat{u}, \tag{2}$$

$$\left(\hat{V}.\hat{\nabla}\right)\hat{T} = \alpha_{nf}\hat{\nabla}^2\hat{T} - \frac{1}{(\rho c_p)_{nf}}\frac{\partial Q_R}{\partial\hat{\gamma}}, \tag{3}$$

$$\rho_{nf} J(\hat{V}.\hat{\nabla})\hat{N} = -\kappa\left(2\hat{N} + \frac{\partial \hat{u}}{\partial \hat{\gamma}} - \frac{\partial \hat{v}}{\partial \hat{\aleph}}\right) + \phi_{nf}\hat{\nabla}^2\hat{N}. \tag{4}$$

where the components $\hat{g}$, $\hat{N}$, $\hat{P}$, and $\hat{V}$ symbolize the gravitational, micro-rotation, pressure, and velocity vectors, respectively, while $\hat{\nabla}^2$, J are called the Laplacian operator, and micro-inertia density, respectively. The momentum equation is divided into two equations in $\hat{\aleph} - \hat{\gamma}$ directions, depending on $\overline{g}$ that can be written as $g_{\aleph} = g\sin(\aleph/a), g_{\gamma} = g\cos(\aleph/a)$, respectively. Also, by applying the boundary approaches of Reynolds number $\mathrm{Re} \to \infty$, which is equivalent to $(1/\mathrm{Re}) \to 0$, and $-(\partial P/\partial \aleph) = u_e(\partial u_e/\partial \aleph)$ (combined convection flow case) [56,57], we can neglect the terms that contain $(1/\mathrm{Re})$. So, the governing non-dimensional equations, in the Cartesian coordinate system are deduced, as follows:

$$\frac{\partial \hat{r}\hat{u}}{\partial\, \hat{\aleph}} + \frac{\partial \hat{r}\hat{v}}{\partial \hat{\gamma}} = 0, \tag{5}$$

$$\begin{aligned} &\hat{u}\frac{\partial \hat{u}}{\partial \hat{\aleph}} + \hat{v}\frac{\partial \hat{u}}{\partial \hat{\gamma}} = \hat{u}_e\frac{d\hat{u}_e}{\partial \hat{\aleph}} + \left(\frac{\mu_{nf}+\kappa}{\rho_{nf}}\right)\frac{\partial^2 \hat{u}}{\partial \hat{\gamma}^2} + \frac{\kappa}{\rho_{nf}}\frac{\partial \hat{N}}{\partial \hat{\gamma}} \\ &+\frac{\left(\chi\rho_s\beta_s+(1-\chi)\rho_f\beta_f\right)}{\rho_{nf}} g(T-T_\infty)\sin\left(\frac{\hat{\aleph}}{a}\right) - \frac{\sigma_{nf}}{\rho_{nf}}B_0^2\hat{u}, \end{aligned} \tag{6}$$

$$\hat{u}\frac{\partial T}{\partial \hat{\aleph}} + \hat{v}\frac{\partial T}{\partial \hat{\gamma}} = \alpha_{nf}\frac{\partial^2 T}{\partial \hat{\gamma}^2} - \frac{1}{(\rho c_p)_{nf}}\frac{\partial Q_R}{\partial \hat{\gamma}}, \tag{7}$$

$$\rho_{nf} J\left(\hat{u}\frac{\partial \hat{N}}{\partial \hat{\aleph}} + \hat{v}\frac{\partial \hat{N}}{\partial \hat{\gamma}}\right) = -\kappa\left(2\hat{N} + \frac{\partial \hat{u}}{\partial \hat{\gamma}}\right) + \phi_{nf}\frac{\partial^2 \hat{N}}{\partial \hat{\gamma}^2}, \tag{8}$$

The nanofluid properties and the radiative heat flux term are defined as follows [42,45]:

$$\begin{aligned} &\alpha_{nf} = \frac{k_{nf}}{(\rho C_p)_{nf}}, \rho_{nf} = (1-\chi_s)\rho_f + \chi_s\rho_s, \mu_{nf} = \frac{\mu_f}{(1-\chi_s)^{2.5}}, \\ &(\rho C_p)_{nf} = (1-\chi_s)(\rho C_p)_f + \chi_s(\rho C_p)_s, \phi_{nf} = \left(\mu_{nf} + \kappa/2\right)j, \\ &\frac{k_{nf}}{k_f} = \frac{(k_s+2k_f)-2\chi_s(k_f-k_s)}{(k_s+2k_f)+\chi_s(k_f-k_s)}, \sigma_{nf} = \left[1 + \frac{3\left((\sigma_s/\sigma_f)-1\right)\chi_s}{\left((\sigma_s/\sigma_f)+2\right)-\left((\sigma_s/\sigma_f)-1\right)\chi_s}\right]\sigma_f, \\ &Q_R = -\frac{4\tau}{3\omega}\frac{\partial T^4}{\partial \hat{\gamma}} = \frac{16\tau}{3\omega}T^3\frac{\partial T}{\partial \gamma}, \end{aligned} \tag{9}$$

where $\hat{u}$ and $\hat{v}$ are components of velocity, χ_s, α_{nf}, μ_{nf}, $\phi_{nf} = (\mu_{nf} + \kappa/2)J$, $(\rho C_p)_{nf}$, B_0 are nanoparticle volume fraction, thermal diffusivity, the viscosity, spin gradient viscosity, heat capacity of the nanofluid, and magnetic field strength, respectively. Also, $\hat{N}$ denotes the microrotation component normal to the $\hat{\aleph} - \hat{\gamma}$ plane. On the other hand, Q_R is called the Rosseland diffusion approximation for radiation, which was offered by Howell et al. [58], such that τ and ω are Stefan–Boltzmann and mean absorption coefficients, respectively. The used boundary conditions for the above system of Equations (5)–(9) are (see [59]):

$$\begin{aligned} &\hat{u} = \hat{v} = 0, T = T_w,\ \hat{N} = -\tfrac{1}{2}\tfrac{\partial \hat{u}}{\partial \hat{\gamma}} \text{ as } \hat{\gamma} = 0, \\ &\hat{u} \to \hat{u}_e(\hat{\aleph}),\ T \to T_\infty \quad \hat{N} \to 0 \text{ as } \hat{\gamma} \to \infty \end{aligned} \tag{10}$$

we see that $\hat{u}_e(\hat{\aleph}) = \frac{3}{2}U_\infty \sin\left(\hat{\aleph}/a\right)$ and $\hat{r}(\hat{\aleph}) = a\sin\left(\hat{\aleph}/a\right)$ are the local free-stream velocity and the radial distance from the symmetrical axis to the surface of the sphere, respectively, and $\hat{u}$ and $\hat{v}$ are called the velocity components along the $\hat{\aleph} - \hat{\gamma}$ plane. The non-dimensional variables are recognized as follows (see [54]):

$$\begin{aligned} &\aleph = \frac{\hat{\aleph}}{a}, \gamma = \mathrm{Re}^{1/4}\left(\frac{\hat{\gamma}}{a}\right), r(\aleph) = \frac{\hat{r}(\hat{\aleph})}{a}, \theta = \frac{T-T_\infty}{T_w-T_\infty}, \\ &u = \frac{\hat{u}}{U_\infty}, v = \mathrm{Re}^{1/2}\left(\frac{\hat{v}}{U_\infty}\right), N = \left(\frac{a}{U_\infty}\right)\mathrm{Re}^{-1/2}\hat{N}, \end{aligned} \tag{11}$$

where $\mathrm{Re} = U_\infty a/v_f$ is the Reynolds number, and v_f is the kinematic viscosity of the fluid.

By substituting the variables included in Equations (9) and (11) in the system (5)–(9), we obtain the following dimensionless system for this problem:

$$\frac{\partial ru}{\partial \aleph} + \frac{\partial ru}{\partial \gamma} = 0, \tag{12}$$

$$\begin{array}{l} u\frac{\partial u}{\partial \aleph} + v\frac{\partial u}{\partial \gamma} = u_e\frac{\partial u_e}{\partial \aleph} + \frac{\rho_f}{\rho_{nf}}(D(\chi_s)+K)\frac{\partial^2 u}{\partial \gamma^2} \\ +\frac{1}{\rho_{nf}}\left(\chi_s\rho_s\left(\frac{\beta_s}{\beta_f}\right)+(1-\chi_s)\rho_f\right)\lambda\theta\sin\aleph + \frac{\rho_f}{\rho_{nf}}K\frac{\partial N}{\partial \gamma} - \frac{\rho_f}{\rho_{nf}}\frac{\sigma_{nf}}{\sigma_f}\mathrm{M}u, \end{array} \tag{13}$$

$$\frac{\mathrm{Pr}}{1+(3/4)\mathrm{L}}\left(u\frac{\partial \theta}{\partial \aleph} + v\frac{\partial \theta}{\partial \gamma}\right) = \left[\frac{k_{nf}/k_f}{(1-\chi_s)+\chi_s(\rho c_p)_s/(\rho c_p)_f}\right]\frac{\partial^2\theta}{\partial \gamma^2}, \tag{14}$$

$$u\frac{\partial N}{\partial \aleph} + v\frac{\partial N}{\partial \gamma} = -\frac{\rho_f}{\rho_{nf}}K\left(2N+\frac{\partial u}{\partial \gamma}\right) + \frac{\rho_f}{\rho_{nf}}\left(D(\chi_s)+\frac{K}{2}\right)\frac{\partial^2 N}{\partial \gamma^2}, \tag{15}$$

here, $D(\chi_s) = 1/(1-\chi_s)^{2.5}$, $\mathrm{Pr} = v_f/\alpha_f$ is the Prandtl number, $K = \kappa/\mu_f$, $\mathrm{M} = (\delta_f B_0^2 a/\rho_f \nu_f)$, $\lambda = Gr/\mathrm{Re}^2$, and $\mathrm{L} = \frac{\alpha\tau(\rho c_p)_{nf}}{4\omega T^3}$ are the micropolar, the magnetic, the mixed convection, and radiation parameters, respectively. In the constant wall temperature boundary conditions case, the Grashof number is given by $Gr = g\beta_f(T_w - T_\infty)\left(a^3/\nu_f^2\right)$. It is important to remember that $\lambda > 0$ for an assisting flow ($T_w > T_\infty$) (heated flow), $\lambda < 0$ for an opposing flow ($T_w < T_\infty$) (cooled flow), and $\lambda = 0$ the forced convection flow.

The non-dimensional boundary conditions are:

$$\begin{array}{c} u = v = 0, \theta = 1, N = -\frac{1}{2}\frac{\partial u}{\partial \gamma} \text{ as } \gamma = 0 \\ u \to u_e(\aleph) = (3/2)\sin\aleph\ u \to 0,\ \theta \to 0,\ N \to 0 \text{ as } \gamma \to \infty. \end{array} \tag{16}$$

To solve Equations (12)–(15), with the boundary conditions (16), suppose we have variables as below [20]:

$$\psi = \aleph r(\aleph) z(\aleph.\gamma), \quad \theta = \theta(\aleph, \gamma), \quad N = \aleph n(\aleph, \gamma)\ , \tag{17}$$

while ψ is the stream function realized as $u = (1/r)(\partial\psi/\partial\gamma)$ and $v = -(1/r)(\partial\psi/\partial\aleph)$, which satisfies the continuity Equation (12). Substituting the Equation (17) into (13) to (15), we acquire the following partial differential equations:

$$\begin{array}{l} \frac{\rho_f}{\rho_{nf}}(D(\chi_s)+K)\frac{\partial^3 z}{\partial \gamma^3} + (1+\aleph\cot\aleph)z\frac{\partial^2 z}{\partial \gamma^2} - \left(\frac{\partial z}{\partial \gamma}\right)^2 + \frac{1}{\rho_{nf}}\left(\chi\rho_s\left(\frac{\beta_s}{\beta_f}\right)+(1-\chi_s)\rho_f\right)\lambda\frac{\sin\aleph}{\aleph}\theta \\ +\frac{9\sin\aleph\cos\aleph}{4\aleph} + \frac{\rho_f}{\rho_{nf}}K\frac{\partial n}{\partial \gamma} - \frac{\rho_f}{\rho_{nf}}\frac{\sigma_{nf}}{\sigma_f}\mathrm{M}z' = \aleph\left(\frac{\partial z}{\partial \gamma}\frac{\partial^2 z}{\partial \aleph \partial \gamma} - \frac{\partial z}{\partial \aleph}\frac{\partial^2 z}{\partial \gamma^2}\right), \end{array} \tag{18}$$

$$\left[\frac{k_{nf}/k_f}{(1-\chi_s)+\chi_s(\rho c_p)_s/(\rho c_p)_f}\right]\frac{\partial^2\theta}{\partial \gamma^2} + \left(\frac{\mathrm{Pr}}{1+(3/4)\mathrm{L}}\right)(1+\aleph\cot\aleph)z\frac{\partial \theta}{\partial \gamma} = \aleph\left(\frac{\partial z}{\partial \gamma}\frac{\partial \theta}{\partial \aleph} - \frac{\partial z}{\partial \aleph}\frac{\partial \theta}{\partial \gamma}\right), \tag{19}$$

$$\frac{\rho_f}{\rho_{nf}}\left(D(\chi_s)+\frac{K}{2}\right)\frac{\partial^2 n}{\partial \gamma^2} + (1+\aleph\cot\aleph)z\frac{\partial n}{\partial \gamma} - \frac{\partial z}{\partial \gamma}n - \frac{\rho_f}{\rho_{nf}}K\left(2n+\frac{\partial^2 z}{\partial \gamma^2}\right) = \aleph\left(\frac{\partial z}{\partial \gamma}\frac{\partial n}{\partial \aleph} - \frac{\partial z}{\partial \aleph}\frac{\partial n}{\partial \gamma}\right), \tag{20}$$

The boundary conditions become:

$$\begin{array}{c} z = \frac{\partial z}{\partial \gamma} = 0, \theta = 1,\ n = -\frac{1}{2}\frac{\partial^2 z}{\partial \gamma^2} \text{ as } \gamma = 0 \\ \frac{\partial f}{\partial \gamma} \to (3/2)(\sin\aleph/\aleph) \quad \theta \to 0,\ n \to 0 \text{ as } \gamma \to \infty \end{array} \tag{21}$$

It can be noticed that at the lower stagnation point of the sphere ($\aleph \approx 0$), equations reduce to the following ordinary differential equations

$$\begin{gathered}\frac{\rho_f}{\rho_{nf}}(D(\chi_s)+K)z'''+2zz''-(z')^2+\\ \frac{1}{\rho_{nf}}\left(\chi_s\rho_s\left(\frac{\beta_s}{\beta_f}\right)+(1-\chi_s)\rho_f\right)\lambda\theta+\frac{9}{4}+\frac{\rho_f}{\rho_{nf}}K\frac{\partial n}{\partial y}-\frac{\rho_f}{\rho_{nf}}\frac{\sigma_{nf}}{\sigma_f}\mathrm{M}z'=0,\end{gathered} \tag{22}$$

$$\left[\frac{k_{nf}/k_f}{(1-\chi_s)+\chi_s(\rho c_p)_s/(\rho c_p)_f}\right]\theta''+2\left(\frac{\mathrm{Pr}}{1+(3/4)\mathrm{L}}\right)z\theta'=0, \tag{23}$$

$$\frac{\rho_f}{\rho_{nf}}\left(D(\chi_s)+\frac{K}{2}\right)n''+2zn'-z'n-\frac{\rho_f}{\rho_{nf}}K(2n+z'')=0. \tag{24}$$

The boundary conditions become:

$$\begin{gathered}z(0)=z'(0)=0,\ \ \theta(0)=1,\ \ n(0)=-\tfrac{1}{2}z''(0)\ \ \text{as}\ \ \gamma=0,\\ z'\to\tfrac{3}{2},\ \ \theta\to 0\,,\ \ n\to 0\ \ \text{as}\ \ \gamma\to\infty,\end{gathered} \tag{25}$$

where primes denote differentiation with respect to γ. Other symbols are defined in the nomenclature section.

The interesting physical quantities, in dimensional form, are local skin friction C_f and Nusselt number Nu, and they can be written as:

$$C_f=\left(\frac{a}{\mu_f U_\infty}\right)\mathrm{Re}^{-1/2}\left((\mu_{nf}+\kappa)\frac{\partial\hat{u}}{\partial\hat{\gamma}}+\kappa\hat{N}\right)_{\hat{\gamma}=0},Nu=\mathrm{Re}^{-1/2}\left(\frac{k_{nf}a}{k_f(T_\infty-T_f)}\frac{\partial T}{\partial\hat{\gamma}}+Q_R\right)_{\hat{\gamma}=0}. \tag{26}$$

Using the non-dimensional variables (11) and boundary conditions (21), local skin friction C_f and Nusselt number Nu are:

$$C_f=\mathrm{Re}^{-1/2}\left(D(\chi_s)+\frac{K}{2}\right)\aleph\frac{\partial^2 z}{\partial\gamma^2}(\gamma,0)\,,Nu=-\mathrm{Re}^{-1/2}(1+\frac{4}{3}L)\left(\frac{k_{nf}}{k_f}\frac{\partial\theta}{\partial\gamma}\right)_{\gamma=0}. \tag{27}$$

3. Numerical Method

The Keller box numerical method is widely applied because it is flexible, much faster, elastically programmable, and efficient, as well as having high accuracy [60–62]. Moreover, given the remarkable nature of the Keller box scheme, some attention should be given to its characteristics and accuracy. The scheme is widely employed in order to be the most adaptable and fixable as compared to other methods. The Keller box method is a significant scheme for solving the convection flow equations, particularly the parabolic equations for the boundary layer models [63,64]. Furthermore, the implicit finite difference scheme (the Keller box method) includes three main techniques, namely, the finite difference method, central differences, and Newton's method, to attain a linear system and solve it via the block tri-diagonal elimination technique [65,66]. The numerical outcomes are obtained by the MATLAB program with excellent results (tables), and smooth curves (figures), and excellent agreement with the previous literature.

Firstly, the Keller box scheme comprises a finite difference method for solving partial differential Equations (18)–(20), which supersedes each of the high derivatives in the differential equation with a first-order equation system, as follows:

$$\begin{gathered}u(\aleph,\gamma)=z'(\aleph,\gamma)\to(u=z')\\ v(\aleph,\gamma)=z''(\aleph,\gamma)\to(v=z''=u')\\ q(\aleph,\gamma)=h'(\aleph,\gamma)\to(q=h')\\ c(\aleph,\gamma)=\theta'(\aleph,\gamma)\to c=\theta',\end{gathered} \tag{28}$$

The differential Equations (18)–(20) to be approximated are:

$$\begin{array}{l}\frac{\rho_f}{\rho_{nf}}\left(\frac{1}{(1-\chi_s)^{2.5}}\right)v' + (1+\aleph\cot\aleph)zv - (u)^2 + \frac{1}{\rho_{nf}}\left((1-\chi_s)\rho_f + \chi_s\frac{\rho_s\beta_s}{\beta_f}\right)\frac{\sin\aleph}{\aleph}\theta \\ + \frac{\rho_f}{\rho_{nf}}Kn' - \frac{\rho_f}{\rho_{nf}}\frac{\sigma_{nf}}{\sigma_f}\mathrm{M}\ u = \aleph\left(u\frac{\partial u}{\partial\aleph} - \frac{\partial z}{\partial\aleph}v\right),\end{array} \tag{29}$$

$$\left(\frac{1+(3/4)\mathrm{L}}{\mathrm{Pr}}\right)\left[\frac{(k_{nf}/k_f)}{(1-\chi_s)+\chi_s(\rho Cp)_s/(\rho Cp)_f]}\right]c' \ + (1+\aleph\cot\aleph)z\frac{\partial\theta}{\partial\gamma} = \aleph\left(z'\frac{\partial\theta}{\partial l} - \frac{\partial z}{\partial l}c\right), \tag{30}$$

$$\frac{\rho_f}{\rho_{nf}}\left(\frac{1}{(1+\chi_s)^{2.5}} + \frac{K}{2}\right)q' + (1+\aleph\cot\aleph)zq - un - \frac{\rho_f}{\rho_{nf}}K(2h+v) = \aleph\left(u\frac{\partial n}{\partial\aleph} - q\frac{\partial z}{\partial\aleph}\right), \tag{31}$$

Such that the prime symbol signalizes the differential of the variable γ. In the same procedure, the boundary conditions (21) will be obtained as:

$$\begin{array}{l}z(\aleph,0) = 0, z(\aleph,0) = 0,\ \theta = 1, \\ z'(\aleph,\infty) = 0,\ \ \theta(\aleph,\infty) = 0,\end{array} \tag{32}$$

To execute the mesh points in the two-dimensional $\aleph$-γ plane, let k^i and g_j be the steps sizes of the relevant step distances in $\aleph$ and γ directions, respectively, as clarified in Figure 2.

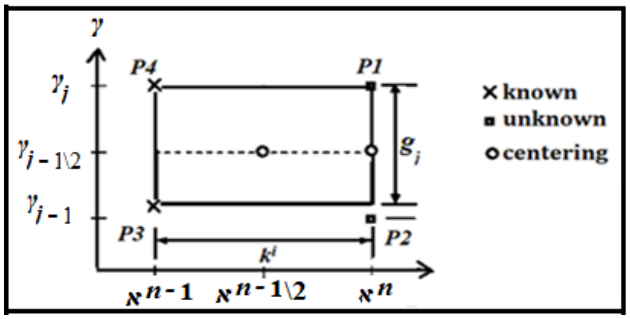

Figure 2. Rectangular net for differential approximations.

In the model that we are investigating, the mesh points are referenced as below:

$$\begin{array}{l}\gamma_0 = 0,\ \ \gamma_i = \gamma_{i-1} + g_i, i = 0,1,2,3,\ldots,J.\gamma_\infty = \gamma_J, \\ \aleph^0 = 0,\ \ \aleph^i = \aleph^i = \aleph^{i-1} + k^i, i = 0,1,2,3,\ldots,N.\end{array} \tag{33}$$

For $i = 1, 2, \ldots, N$, $j = 1, 2, \ldots, J$, the midpoint and first derivative for these quantities, can be obtained at the inner mesh points ( ) as follows:

$$\begin{array}{c}()^{n-1/2}_{j-1/2} = \frac{1}{4}\left()^n_j + ()^n_{j-1} + ()^{n-1}_j + ()^{n-1}_{j-1}\right) \\ \left(\frac{\partial()}{\partial\gamma}\right)^{n-1/2}_{j-1/2} = \frac{1}{2g_j}\left()^n_j - ()^n_{j-1} + ()^{n-1}_j - ()^{n-1}_{j-1}\right) \\ \left(\frac{\partial()}{\partial\aleph}\right)^{n-1/2}_{j-1/2} = \frac{1}{2k^n}\left()^n_j - ()^n_{j-1} + ()^{n-1}_j - ()^{n-1}_{j-1}\right),\end{array} \tag{34}$$

Consequently, the systems of Equations (24) and (25)–(27) are extracted at the midpoint ($\aleph$, $\gamma_{j-1/2}$), which is called "centering", as the form:

$$z^n_j - z^n_{j-1} = g_j\left(u^n_{j-1/2}\right), \tag{35}$$

$$u^n_j - u^n_{j-1} = g_j\left(v^n_{j-1/2}\right), \tag{36}$$

$$\theta_j^n - \theta_{j-1}^n = g_j\left(q_{j-1/2}^n\right), \tag{37}$$

$$\begin{aligned}&\frac{\rho_f}{\rho_{nf}}\left(\frac{1}{(1-\chi_s)^{2.5}}\right)(v_j - v_{j-1}) + (1+\xi+\aleph\cot\aleph)\tfrac{\xi}{4}g_j(z_j+z_{j-1})(v_j+v_{j-1}) - \left(\tfrac{1+\xi}{4}\right)g_j\,(u_j+u_{j-1})^2 -\\ &\tfrac{1}{2}\frac{\rho_f\sigma_{nf}}{\rho_{nf}\sigma_f}\,\mathrm{M}g_j\,(u_j+u_{j-1}) + \left(\tfrac{1+\xi}{2}\right)g_j v_{j-1/2}^{n-1}(z_j+z_{j-1}) - \left(\tfrac{1+\xi}{2}\right)g_j z_{j-1/2}^{n-1}(v_j+v_{j-1}) +\\ &\tfrac{1}{2}\frac{1}{\rho_{Hnf}}\left((1-\chi_s)\rho_f + \chi_s\frac{\rho_s\beta_s}{\beta_f}\right)\frac{\sin\aleph^{n-1/2}}{\aleph^{n-1/2}}g_j(\theta_j+\theta_{j-1}) + \frac{\rho_f}{\rho_{nf}}K\left(\tfrac{1+\xi}{2}\right)(n_j - n_{j-1})) = (L_1)_{j-1/2}^{n-1}\end{aligned} \tag{38}$$

$$\begin{aligned}&\left(\tfrac{1+(3/4)\mathrm{L}}{\mathrm{Pr}}\right)\left[\frac{k_{nf}/k_f}{(1-\chi_s)+\chi_s(\rho Cp)_s/(\rho Cp)_f}\right]\left(q_j - q_{j-1}\right) -\\ &\tfrac{\xi}{4}g_j(u_j+u_{j-1}^n)(\theta_j+\theta_{j-1}) + (1+\xi+\aleph\cot\aleph)\tfrac{1}{4}g_j(z_j+z_{j-1})(q_j+q_{j-1}) + \tfrac{\xi}{2}g_j(u_j+u_{j-1})\theta_{j-1/2}^{n-1} -\\ &\tfrac{\xi}{2}g_j u_{j-1/2}^{n-1}(\theta_j+\theta_{j-1}) - \tfrac{\xi}{2}g_j(q_j-q_{j-1})z_{j-1/2}^{n-1} + \tfrac{\xi}{2}g_j q_{j-1/2}^{n-1}(z_j+z_{j-1}) = (L_2)_{j-1/2}^{n-1}\end{aligned} \tag{39}$$

$$\begin{aligned}&\tfrac{\rho_f}{\rho_{nf}}\left(D(\chi_s)+\tfrac{K}{2}\right)(q_j-q_{j-1}) + \tfrac{(1+\xi)}{4}g_j(z_j-z_{j-1})(q_j-q_{j-1}) -\\ &\tfrac{(1+\xi)}{4}(u_j-u_{j-1})(n_j-n_{j-1}) - \tfrac{\rho_f}{\rho_{nf}}\tfrac{\xi}{2}Kg_j(n_j+n_{j-1}) - \tfrac{\rho_f}{\rho_{nf}}\tfrac{\xi}{2}Kg_j(v_j+v_{j-1}) \\ &+\tfrac{\xi}{2}g_j n_{j-1/2}^{n-1}(u_j+u_{j-1}) - \tfrac{\xi}{2}g_j u_{j-1/2}^{n-1}(n_j+n_{j-1}) = (L)_3^{n-1},\end{aligned} \tag{40}$$

$$(L_1)_{j-1/2}^{n-1} = -g_j\begin{pmatrix} \frac{\rho_f}{\rho_{nf}}\left(\frac{1}{(1-\chi_s)^{2.5}}\right)\frac{\left(v_j-v_{j-1}\right)}{g_j} + (1-\xi)z_{j-1/2}v_{j-1/2} + (\xi-1)\left(u_{j-1/2}\right)^2 \\ -\frac{\rho_f\sigma_{nf}}{\rho_{nf}\sigma_f}\,\mathrm{M}u_{j-1/2} + \left((1-\chi_s)+\chi_s\frac{\rho_{s1}\beta_{s1}}{\beta_f}\right)\frac{\sin\aleph^{n-1/2}}{\aleph^{n-1/2}}\theta_{j-1/2} + \frac{\rho_f}{\rho_{nf}}K\;q_{j-1/2}\end{pmatrix}^{n-1} \tag{41}$$

$$(L_2)_{j-1/2}^{n-1} = -g_j\begin{pmatrix}\left(\frac{1+(3/4)\mathrm{L}}{\mathrm{Pr}}\right)\left[\frac{k_{nf}/k_f}{(1-\chi_s)+\chi_s(\rho Cp)_s/(\rho Cp)_f}\right]\frac{\left(q_j-q_{j-1}\right)}{g_j} \\ +(1+\aleph\cot\aleph-\xi)z_{j-1/2}q_{j-1/2} + \xi u_{j-1/2}\theta_{j-1/2}\end{pmatrix}^{n-1} \tag{42}$$

$$(L_1)_{j-1/2}^{n-1} = -g_j\begin{pmatrix}\frac{\rho_f}{\rho_{nf}}\left(\frac{1}{(1-\chi_s)^{2.5}}+\frac{K}{2}\right)(q_j-q_{j-1}) + (1-\xi)z_{j-1/2}q_{j-1/2} \\ +(\xi-1)\left(n_{j-1/2}u_{j-1/2}\right) - \frac{\rho_f}{\rho_{nf}}K(n_{j-1/2}+v_{j-1/2})\end{pmatrix}^{n-1} \tag{43}$$

where $\xi = \frac{\aleph^{n-1/2}}{k^i}$

The boundary condition can be expressed as:

$$z_0^n = u_0^n = 0,\ \theta_0^n = 1, u_J^n = \theta_J^n = 0, \tag{44}$$

4. Validation of Numerical Findings

The governing Equations (14)–(16), subject to the boundary conditions (17), were solved numerically using the Keller box method presented by [67]. Before determining the effects of micropolar nanofluid, the values of Cf should be compared to those given by Nazar and Pop [68] at K = 0, $\chi_s = 0$, M = 0, and L = 0, as displayed in Table 1. It is found that the values of C_f are in perfect agreement.

Table 1. Values of C_f for K $= 0$ $\chi_s = 0$, M = 0, and L = 0 (Newtonian fluid), Pr = 0.7, and various values of λ.

ℵ	λ							
	−4	**−3**	**−2**	**−1**	**−0.5**	**0.0**	**0.74**	**0.75**
0°	(0.0000)	(0.0000)	(0.0000)	(0.0000)	(0.0000)	(0.0000)	(0.0000)	(0.0000)
	(0.0000)	(0.0000)	(0.0000)	(0.0000)	(0.0000)	(0.0000)	(0.0000)	(0.0000)
10°	0.07899	0.1794	0.2627	0.3401	0.3768	0.4146	0.46221	0.4631
	(0.0801)	(0.1806)	(0.2662)	(0.3438)	(0.3804)	(0.4160)	(0.4669)	(0.4675)
20°	0.11270	0.3240	0.4981	0.6522	0.7277	0.7967	0.8898	0.9004
	(0.1149)	(0.3261)	(0.5000)	(0.6564)	(0.7301)	(0.8014)	(0.9031)	(0.9045)
30°		0.3890	0.6669	0.8998	1.0009	1.1767	1.2754	1.2736
		(0.4024)	(0.6718)	(0.9098)	(1.0211)	(1.1284)	(1.2813)	(1.2833)
40°		0.3609	0.7509	1.0726	1.2003	1.3689	1.5740	1.5721
		(0.3704)	(0.7535)	(1.0790)	(1.2292)	(1.3733)	(1.5775)	(1.5802)
50°			0.7109	1.14780	1.3015	1.4782	1.7700	1.7715
			(0.7181)	(1.1434)	(1.3350)	(1.5172)	(1.7737)	(1.7771)
60°			0.5226	1.1047	1.2890	1.4518	1.8536	1.8561
			(0.5295)	(1.0866)	(1.3246)	(1.4577)	(1.8580)	(1.8621)
70°				0.8899	1.1870	1.4539	1.8222	1.8270
				(0.8929)	(1.1889)	(1.4583)	(1.8260)	(1.8307)
80°				0.5093	0.9113	1.2403	1.6741	1.6802
				(0.5280)	(0.9190)	(1.2480)	(1.6800)	(1.6855)
90°					0.4735	0.9100	1.4224	1.4317
					(0.4813)	(0.9154)	(1.4289)	(1.4352)
100°						0.4119	1.0745	1.0477
						(0.4308)	(1.0847)	(1.0922)
110°							0.6141	0.6000
							(0.6543)	(0.6637)
120°								0.0079
								(0.0380)

5. Graphical Findings and Discussion

MATLAB software assisted in obtaining graphical outcomes for several values of micropolar nanofluid parameters for the physical quantities, such as C_f, Nu, $\theta(0,\gamma)$, $z'(0,\gamma)$, and $h(0,\gamma)$ at various positions ℵ, for the assisting $(\lambda > 0)$ and opposing $(\lambda < 0)$ flow. The data regarding the thermo–physical characteristics of the used fluid and nanoparticles are listed in Table 2.

Table 2. Thermo–physical properties of based fluids and nanoparticles [37,43,69].

Material	**ρ(kg/m^3)**	**ρC_p(J/kgK)**	**k(W/mK)**	**B $\times$ 10^{-5}K^{-1}**	**σ (s/m)**	**Pr**
Water	997.1	4179	0.613	21	5.5×10^{-6}	6.2
Methanol	792	2545	0.2035	149	5×10^{-7}	7.3
Al_2O_3	3970	765	40	0.85	3.5×10^{7}	...
CuO	6510	540	18	0.85	3.96×10^{7}	...

Figures 3 and 4 visualize the influence of the magnetic field factor on both skin friction and Nusselt number. It is noticeable that the increment in the magnetic field parameter M leads directly to a decrease in both skin friction and Nusselt number. This could be due to the restriction in nanofluid flow, as a result of the Lorentz force formation caused by an increase in the strength of the magnetic field, which, in turn, acts to curb energy transport and skin friction. Figures 5 and 6 are plotted to describe the extent of the domination of the volume fraction of nanoparticles χ_s on skin friction and Nusselt number, respectively. It is well-known that the increasing value of nanoparticle volume fraction improves the thermal conductivity of the nanoliquid. This, of course, improves the transfer of energy between the spherical surface and the nanoliquid, in addition to reducing the friction force,

resulting in an elevation of the curves of Nusselt number, and a lowering of the curves of skin friction. The effect of micropolar parameter K on skin friction and Nusselt number is reported in Figures 7 and 8, respectively. It is observed that K has an inverse relationship with C_f and Nu. Actually, the gain in micropolar factor raises nanofluid viscosity, which decreases both the Nusselt number and skin friction. Figures 9 and 10 show how the skin friction and Nusselt number are affected by the combined convection parameter λ, respectively. It is obvious that the gain in the mixed convection coefficient increases buoyant forces that enhance momentum transfer, thereby increasing the energy transport rate and friction drag. It is also worth noting that moving from a cooling ($\lambda < 0$) state to a heating state ($\lambda > 0$) contributes to changing the behavior of micropolar nanofluid, in which Al_2O_3–H_2O changes its behavior, as it possesses the lowest value for skin friction upon cooling, and has the highest value for skin friction upon heating. Figures 11 and 12 focus on showing the effect of the radiation parameter L on the Nusselt number and skin friction, respectively. Releasing more thermal radiation means more heat is added to the micropolar liquid. In other words, the radiation parameter acts as an additional heat source, and this increases the effectiveness of energy transfer and enhances the forces of friction. Moreover, in Figures 3–12, it is found that the Nusselt number has its greatest value when methanol (CH_3OH) is used as a base fluid, due to its lower value of thermal conductivity (Table 1), which plays a critical role in raising the Nusselt number, as seen in Equation (18).

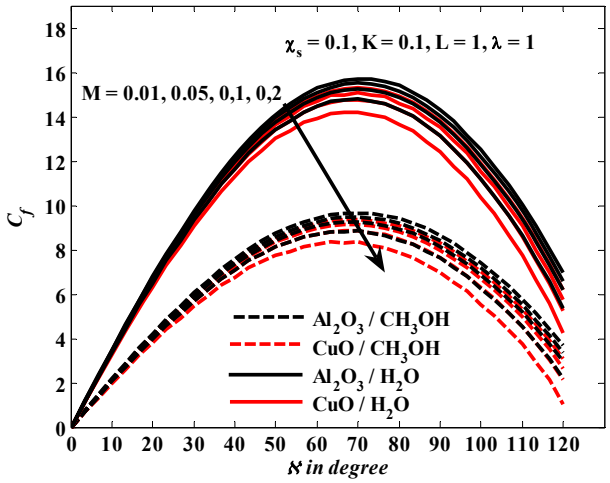

Figure 3. Flow properties for C_f vs. different values of ℵ and M.

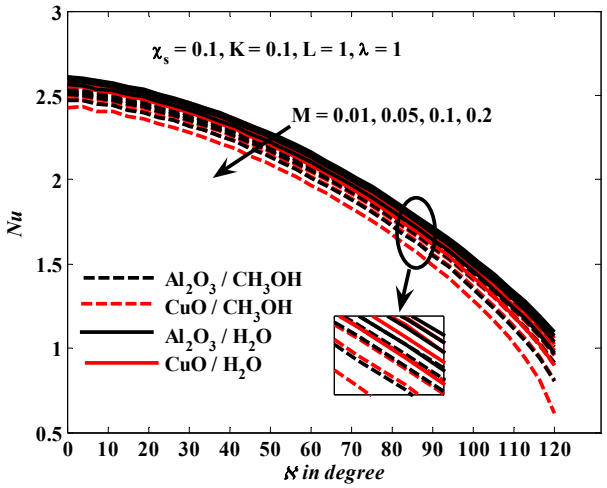

Figure 4. Flow properties for Nu vs. different values of ℵ and M.

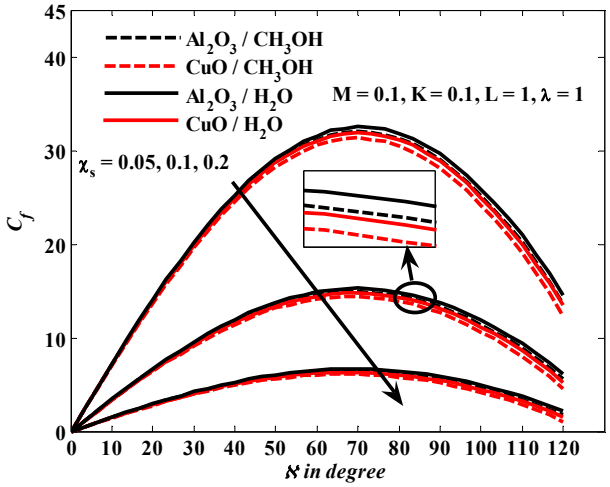

Figure 5. Flow properties for C_f vs. different values of ℵ and χ_s.

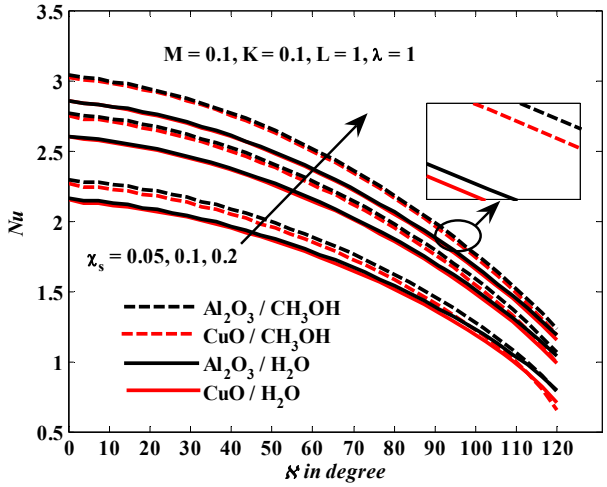

Figure 6. Flow properties for Nu vs. different values of ℵ and χ_s.

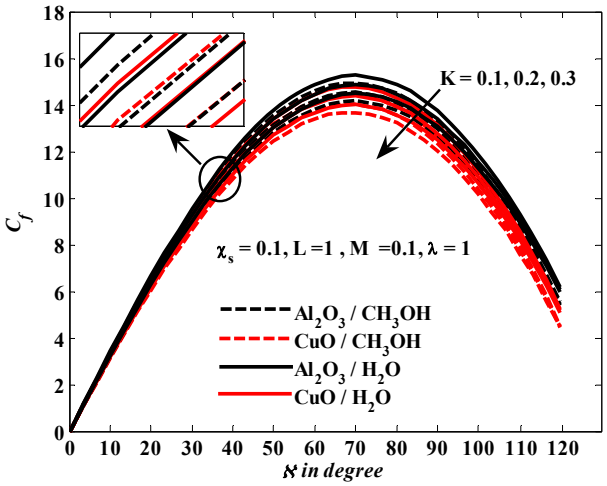

Figure 7. Flow properties for C_f vs. different values of ℵ and K.

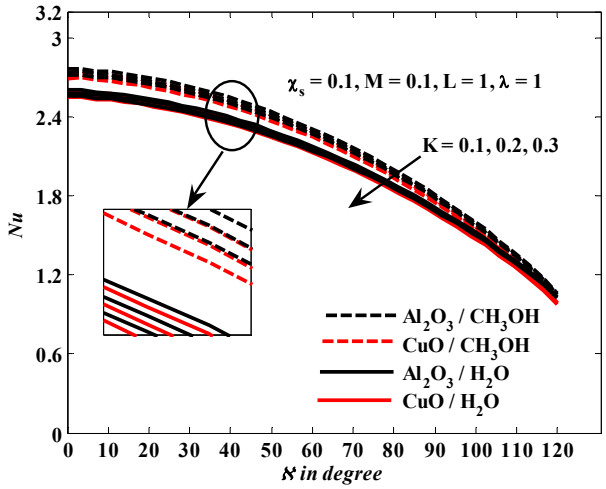

Figure 8. Flow properties for *Nu* vs. different values of ℵ and K.

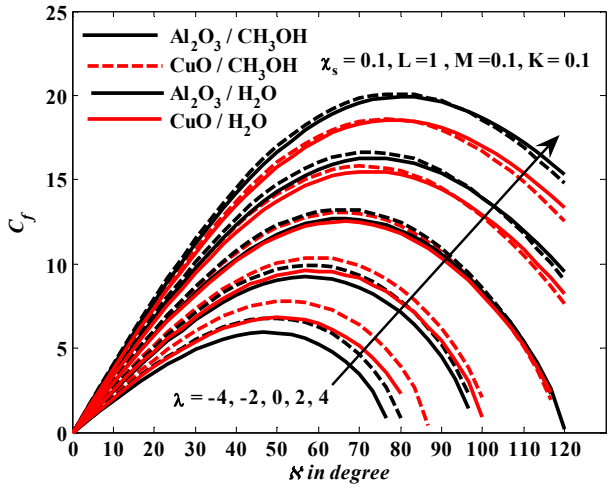

Figure 9. Flow properties for C_f vs. different values of ℵ and λ.

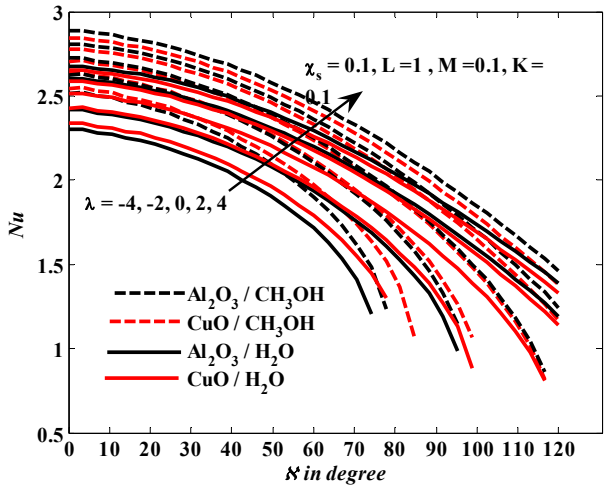

Figure 10. Flow properties for *Nu* vs. different values of ℵ and λ.

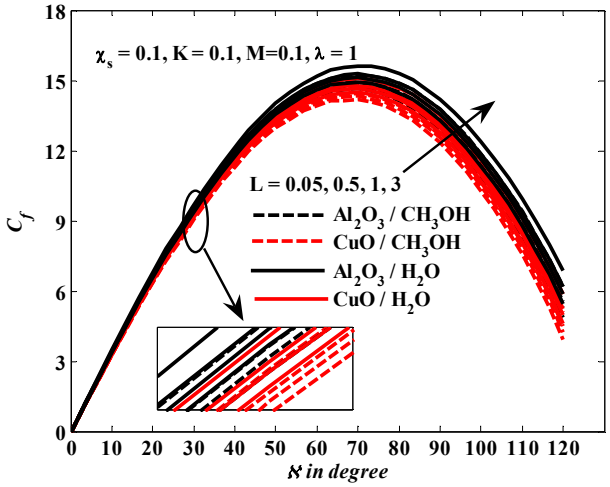

Figure 11. Flow properties for C_f vs. different values of ℵ and L.

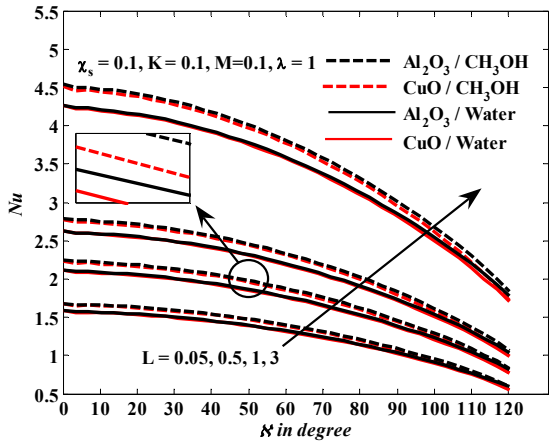

Figure 12. Flow properties for *Nu* vs. different values of ℵ and L.

The impact of changing the parameters M, χ_s, K, λ, and L on the temperature θ, velocity $\partial z/\partial \gamma$, and angular velocity h is investigated separately in Figures 13–27. According to Figures 13–15, increasing the magnetic field strength causes a rise in temperature, as well as a decline in velocity and angular velocity. The formation of the Lorentz force, which is created by the crossing of a magnetic field through a moving fluid, is the reason behind these behaviors. This force increases the fluid's resistance to movement, and raises its temperature. Figures 16–18 show the responses of temperature, velocity, and angular velocity to the effect of the volume fraction of nanoparticles χ_s, respectively. It is well-known that the increase in the volume fraction of the nanoparticles contributes to an increase in the rate of energy transfer. Furthermore, the collision of ultrafine particles in the flow generates more thermal energy and, thus, raises the temperature of the nanofluid. Simultaneously, the increase in χ_s increases the density of the fluid, impeding its movement. According to Figures 19–21, the volume fraction of the nanoparticles and the micropolar parameter have the same effect, in that the profiles of temperature, velocity, and angular velocity show the same impression. The temperature rises as it rises, while velocity and angular velocity decline. This actually occurs because raising the micropolar parameter raises the viscosity of the nanofluid. Figures 22–24 indicate the effects of increasing the mixed convection parameter on the temperature, velocity, and angular velocity, respectively. As a result of the increase in mixed convection parameter, the buoyant forces are boosted, which makes the temperature profiles decrease, and the velocity and angular velocity of the nanofluid increase. Furthermore, the physical quantities of the micropolar nanofluid can completely change from cooling ($\lambda < 0$) to heating ($\lambda > 0$) states, with Al_2O_3–H_2O having

the highest velocity and angular velocity at heating, but it has the lowest value of the same two physical quantities at cooling compared to the other nanofluids studied. Figures 25–27 are plotted to examine the effect of the thermal radiation parameter L on the profiles of temperature, angular velocity, and velocity. It is clear that increasing the radiation parameter raises the temperature of the micropolar fluid, and increases both the angular velocity and the velocity. An explanation for this behavior may be that an increase in the rate of radiation causes more energy to be released into the micropolar liquid, and this, of course, improves the mentioned physical quantities. Through the study of the different parameters that act on the temperature profiles, it is seen that the CuO–H_2O micropolar nanofluid acquires the top value of the temperature profile when compared with the other micropolar nanofluids. The physical properties of the copper oxide used as a nanoparticle could be the main reason for the high temperatures, such as the lower thermal conductivity and higher density of CuO.

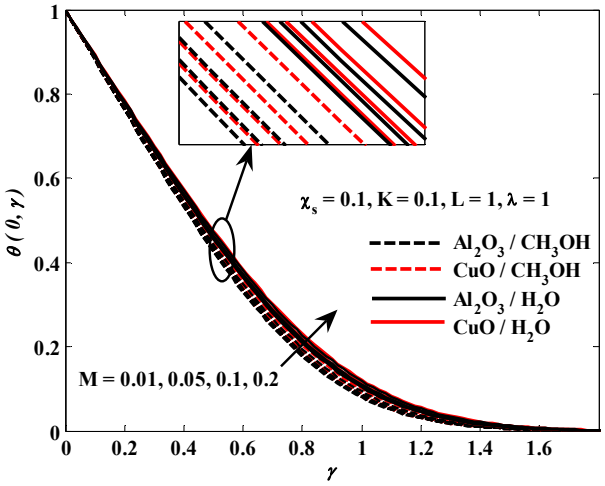

Figure 13. Flow properties for temperature vs. different values of γ and M.

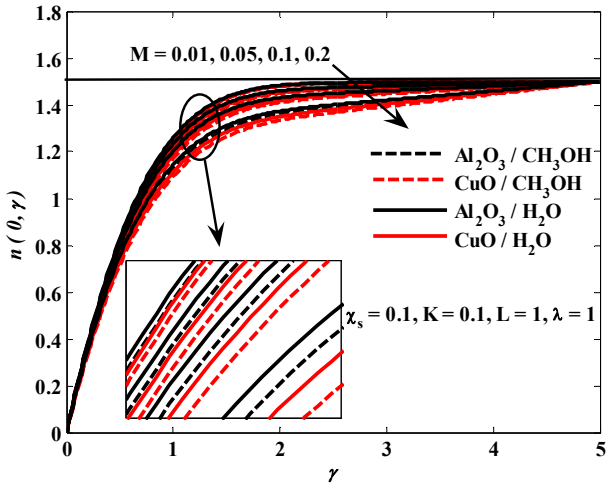

Figure 14. Flow properties for angular velocity vs. different values of γ and M.

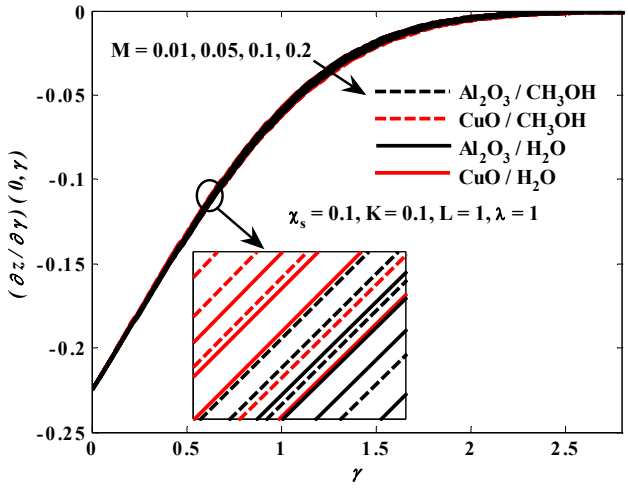

Figure 15. Flow properties for velocity vs. different values of γ and M.

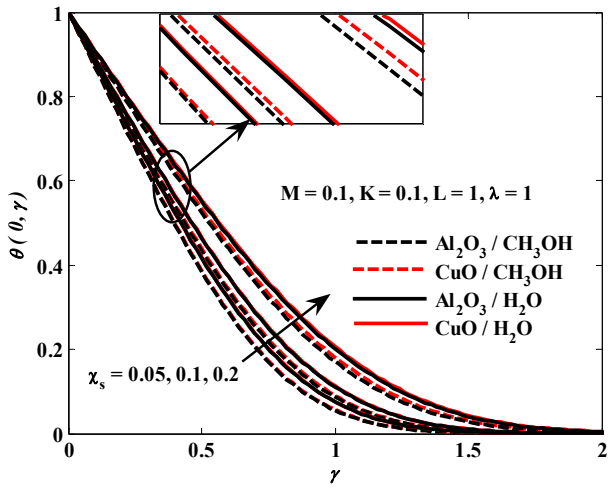

Figure 16. Flow properties for velocity vs. different values of γ and χ_s.

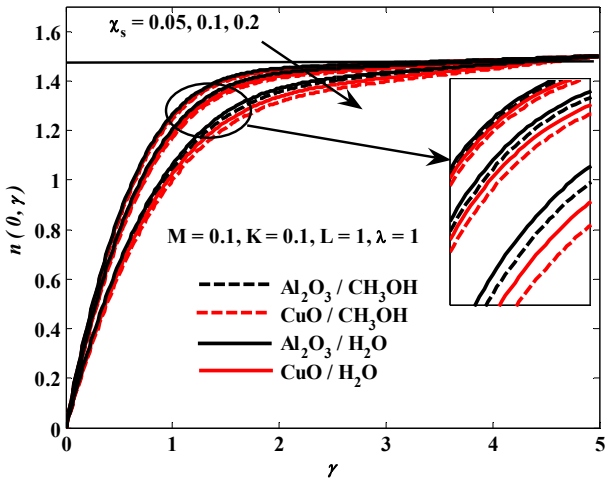

Figure 17. Flow properties for angular velocity vs. different values of γ and χ_s.

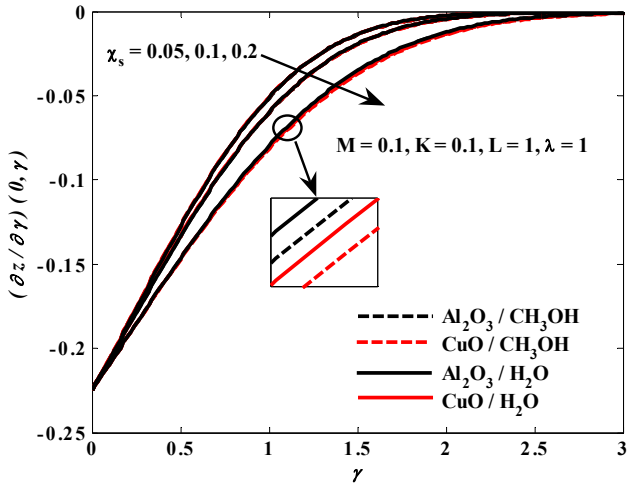

Figure 18. Flow properties for velocity vs. different values of γ and χ_s.

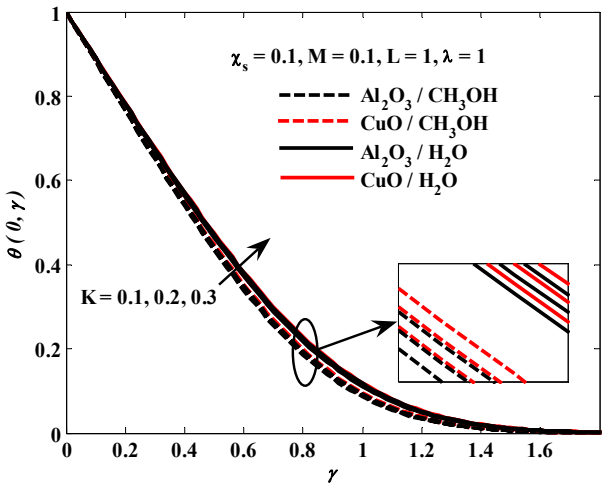

Figure 19. Flow properties for temperature vs. different values of γ and K.

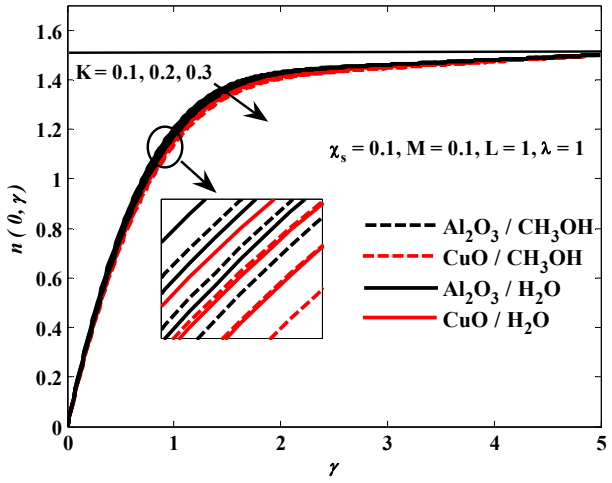

Figure 20. Flow properties for angular velocity vs. different values of γ and K.

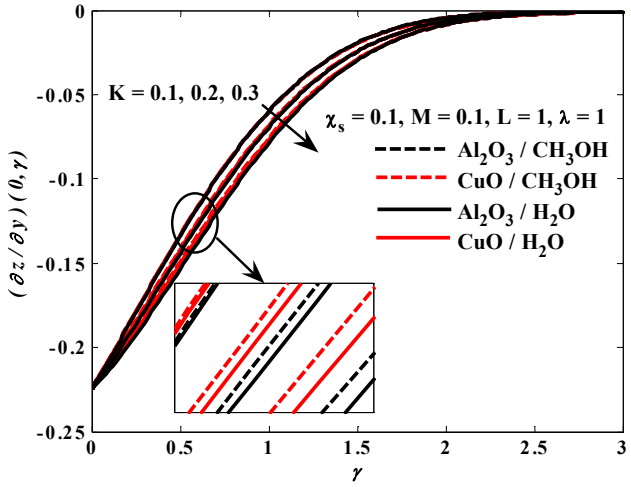

Figure 21. Flow properties for velocity vs. different values of γ and K.

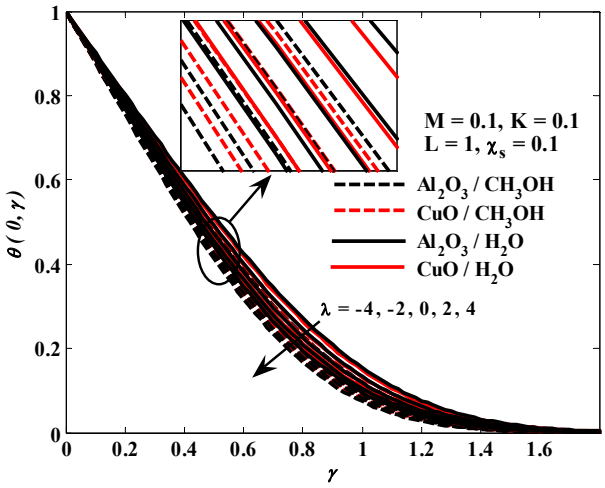

Figure 22. Flow properties for temperature vs. different values of γ and λ.

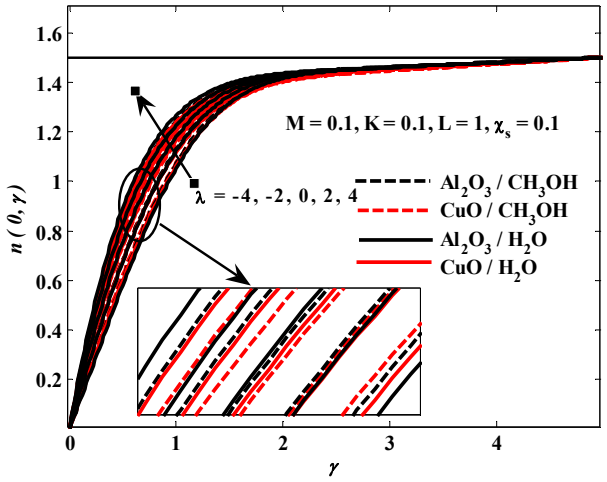

Figure 23. Flow properties for angular velocity vs. different values of γ and λ.

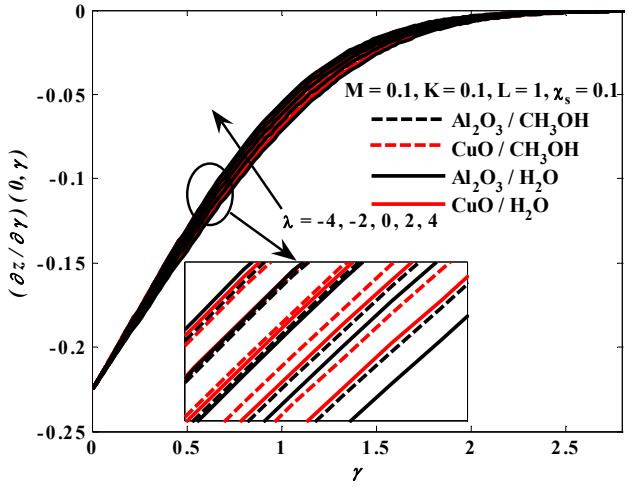

Figure 24. Flow properties for velocity vs. different values of γ and λ.

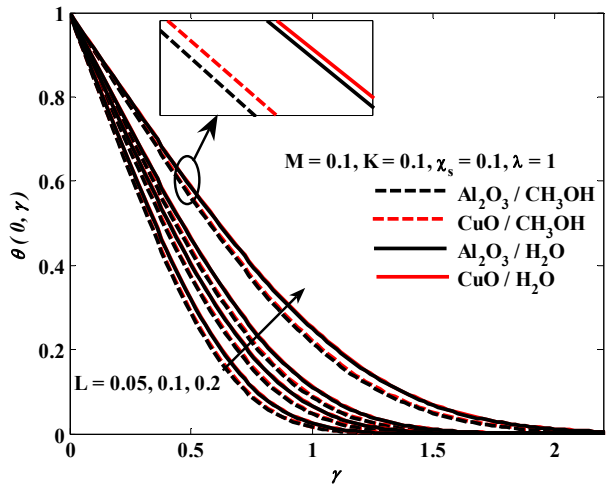

Figure 25. Flow properties for temperature vs. different values of γ and L.

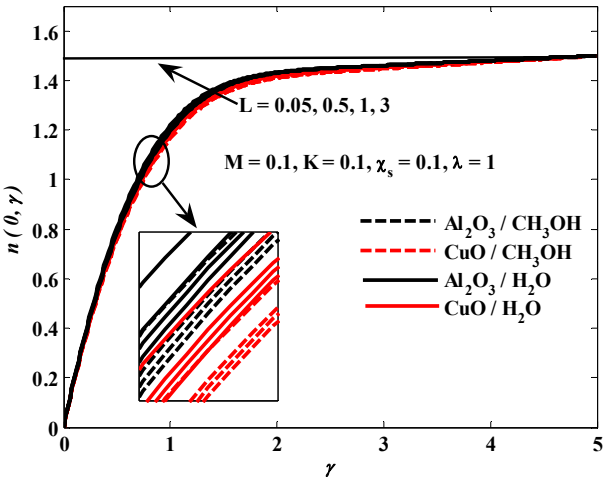

Figure 26. Flow properties for angular velocity vs. different values of γ and L.

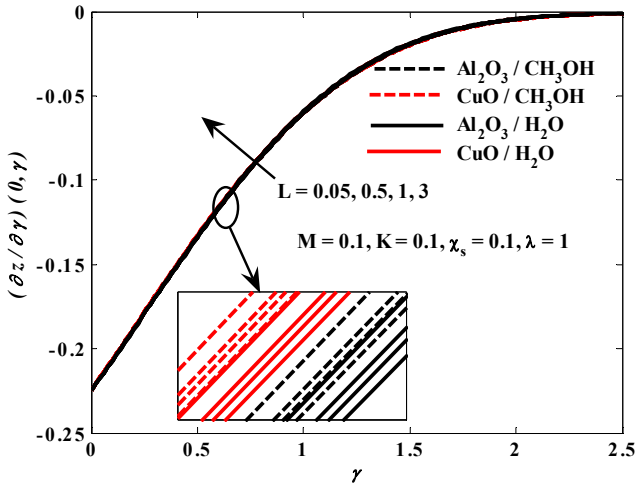

Figure 27. Flow properties for of velocity vs. different values of γ and L.

6. Conclusions

The existing work is concerned with the impression of thermal radiation on the heat transfer characteristics of a magnetized micropolar nanofluid flowing around a spherical surface. To this end, a governing model was constructed, based on the Tiwari–Das nanofluid model, and solved numerically through the Keller box method. The following points focus on the main results:

1. The use of aluminum oxide (Al_2O_3) as a nanoparticle in nanofluids always shows the highest values of physical quantities, such as local skin friction, Nusselt number, velocity, and angular velocity compared to copper oxide (CuO) nanoparticles, but for the temperature profile, it tends to favor copper oxide, which occupies the top of the temperature values;
2. Nanoparticles suspended in water as a base fluid obtain higher values for measurements of local skin friction, temperature, velocity, and angular velocity compared to an ethanol base fluid. However, ethanol had the highest values for the Nusselt number compared to water;
3. The mixed convection and radiation parameters are the only two parameters that raise the quantities of local skin friction, velocity, and angular velocity by their increment;
4. Raising the values of the M, χ_s, and K, parameters is responsible for promoting the temperature, but the mixed convection parameter is not included in this behavior. Its increment causes a decrease in temperature;
5. The Nusselt number is directly proportional to each volume parameter and mixed convection parameter, while it is inversely proportional to the magnetic parameter and micropolar parameter.

Author Contributions: Conceptualization, M.Z.S.; modeling, analysis, and results, F.S.; investigation, F.A.A.; discussions and writing literature, M.A.H.I.; resources, I.M.S.; writing draft, N.Y.; formal analysis, and M.F.M.N.; software. All authors have read and agreed to the published version of the manuscript.

Funding: This manuscript is supported by the Faculty of Entrepreneurship and Business, Universiti Malaysia Kelantan, Kelantan, Malaysia.

Institutional Review Board Statement: Not applicable.

Informed Consent Statement: Not applicable.

Data Availability Statement: Not applicable.

Acknowledgments: The authors are thankful to the Faculty of Entrepreneurship and Business, Universiti Malaysia Kelantan, Kelantan, Malaysia for their support.

Conflicts of Interest: The authors declare no conflict of interest.

Nomenclature

a	Radius of spherical shape	U_∞	Uniform-free stream
B_o	Magnetic field strength	γ	Y-component of velocity
C_f	Skin friction coefficient	v_f	Kinematic viscosity of host liquid
(C_p)	Heat capacity	Greek symbols	
$z\ (x, y)$	Dimensionless stream function	α	Thermal diffusivity coefficient
g	Gravity vector	β	Thermal expansion of host liquid
Gr	Grashof number	σ	Electrical conductivity
J	Micro-inertia density	θ	Temperature of nanoliquid
k_f	Thermal conductivity	κ	Vortex viscosity
M	Magnetic parameter	λ	Combined convection parameter
Nu	Nusselt number	μ	Dynamic viscosity
P	Fluid pressure	ρ	Density
Pr	Prandtl number	ϕ	Spin gradient viscosity
Q_R	Rosseland diffusion approximation	χ_s	Nanosolid volume fraction
Re	Reynold number	ψ	Stream transformation
T	Temperature of the fluid	Subscript	
T_∞	Ambient temperature	f	Host liquid
$\aleph$	x-component of velocity	nf	Nanoliquid
$u_e(x)$	Free-stream velocity	s	Nanosolid

References

1. Choi, S.U.; Eastman, J.A. *Enhancing Thermal Conductivity of Fluids with Nanoparticles*; Argonne National Lab.: San Francisci, CA, USA, 1995.
2. Eastman, J.A.; Choi, S.; Li, S.; Yu, W.; Thompson, L. Anomalously increased effective thermal conductivities of ethylene glycol-based nanofluids containing copper nanoparticles. *Appl. Phys. Lett.* **2001**, *78*, 718–720. [CrossRef]
3. Xuan, Y.; Li, Q. Heat transfer enhancement of nanofluid. *Int. J. Heat Fluid Flow* **2000**, *21*, 58–64. [CrossRef]
4. Yu, W.; France, D.M.; Routbort, J.L.; Choi, S.U. Review and comparison of nanofluid thermal conductivity and heat transfer enhancements. *Heat Transf. Eng.* **2008**, *29*, 432–460. [CrossRef]
5. Kakaç, S.; Pramuanjaroenkij, A. Review of convective heat transfer enhancement with nanofluids. *Int. J. Heat Mass Transf.* **2009**, *52*, 3187–3196. [CrossRef]
6. Lee, S.; Choi, S.U. *Application of Metallic Nanoparticle Suspensions in Advanced Cooling Systems*; Argonne National Lab.: Chicago, IL, USA, 1996.
7. Pandya, N.S.; Shah, H.; Molana, M.; Tiwari, A.K. Heat transfer enhancement with nanofluids in plate heat exchangers: A comprehensive review. *Eur. J. Mech.-B Fluids* **2020**, *81*, 173–190. [CrossRef]
8. Kumar, A.; Subudhi, S. Preparation, characterization and heat transfer analysis of nanofluids used for engine cooling. *Appl. Therm. Eng.* **2019**, *160*, 114092. [CrossRef]
9. Du, R.; Jiang, D.; Wang, Y.; Shah, K.W. An experimental investigation of CuO/water nanofluid heat transfer in geothermal heat exchanger. *Energy Build.* **2020**, *227*, 110402. [CrossRef]
10. Deriszadeh, A.; de Monte, F. On heat transfer performance of cooling systems using nanofluid for electric motor applications. *Entropy* **2020**, *22*, 99. [CrossRef]
11. Buongiorno, J.; Hu, L.-w. Nanofluid heat transfer enhancement for nuclear reactor applications. In Proceedings of the International Conference on Micro/Nanoscale Heat Transfer, Shanghai, China, 18–21 December 2009; pp. 517–522.
12. Khanafer, K.; Vafai, K.; Lightstone, M. Buoyancy-driven heat transfer enhancement in a two-dimensional enclosure utilizing nanofluids. *Int. J. Heat Mass Transf.* **2003**, *46*, 3639–3653. [CrossRef]
13. Buongiorno, J. Convective transport in nanofluids. *J. Heat Transf.* **2006**, *128*, 240–250. [CrossRef]
14. Tiwari, R.K.; Das, M.K. Heat transfer augmentation in a two-sided lid-driven differentially heated square cavity utilizing nanofluids. *Int. J. Heat Mass Transf.* **2007**, *50*, 2002–2018. [CrossRef]
15. Ho, C.-J.; Chen, M.; Li, Z. Numerical simulation of natural convection of nanofluid in a square enclosure: Effects due to uncertainties of viscosity and thermal conductivity. *Int. J. Heat Mass Transf.* **2008**, *51*, 4506–4516. [CrossRef]
16. Nield, D.; Kuznetsov, A. The Cheng–Minkowycz problem for natural convective boundary-layer flow in a porous medium saturated by a nanofluid. *Int. J. Heat Mass Transf.* **2009**, *52*, 5792–5795. [CrossRef]
17. Kuznetsov, A.; Nield, D. The Cheng–Minkowycz problem for natural convective boundary layer flow in a porous medium saturated by a nanofluid: A revised model. *Int. J. Heat Mass Transf.* **2013**, *65*, 682–685. [CrossRef]

18. Das, S.; Chakraborty, S.; Jana, R.; Makinde, O. Entropy analysis of unsteady magneto-nanofluid flow past accelerating stretching sheet with convective boundary condition. *Appl. Math. Mech.* **2015**, *36*, 1593–1610. [CrossRef]
19. Shahid, A.; Zhou, Z.; Bhatti, M.; Tripathi, D. Magnetohydrodynamics nanofluid flow containing gyrotactic microorganisms propagating over a stretching surface by successive Taylor series linearization method. *Microgravity Sci. Technol.* **2018**, *30*, 445–455. [CrossRef]
20. Alwawi, F.A.; Alkasasbeh, H.T.; Rashad, A.M.; Idris, R. A numerical approach for the heat transfer flow of carboxymethyl cellulose-water based Casson nanofluid from a solid sphere generated by mixed convection under the influence of Lorentz force. *Mathematics* **2020**, *8*, 1094. [CrossRef]
21. Azam, M.; Xu, T.; Khan, M. Numerical simulation for variable thermal properties and heat source/sink in flow of Cross nanofluid over a moving cylinder. *Int. Commun. Heat Mass Transf.* **2020**, *118*, 104832. [CrossRef]
22. Qaiser, D.; Zheng, Z.; Khan, M.R. Numerical assessment of mixed convection flow of Walters-B nanofluid over a stretching surface with Newtonian heating and mass transfer. *Therm. Sci. Eng. Prog.* **2021**, *22*, 100801. [CrossRef]
23. Khan, U.; Zaib, A.; Ishak, A.; Sherif, E.-S.M.; Waini, I.; Chu, Y.-M.; Pop, I. Radiative mixed convective flow induced by hybrid nanofluid over a porous vertical cylinder in a porous media with irregular heat sink/source. *Case Stud. Therm. Eng.* **2022**, *30*, 101711. [CrossRef]
24. Chabani, I.; Mebarek-Oudina, F.; Ismail, A.A.I. MHD Flow of a Hybrid Nano-fluid in a Triangular Enclosure with Zigzags and an Elliptic Obstacle. *Micromachines* **2022**, *13*, 224. [CrossRef] [PubMed]
25. Uddin, M.S.; Bhattacharyya, K.; Shafie, S. Micropolar fluid flow and heat transfer over an exponentially permeable shrinking sheet. *Propuls. Power Res.* **2016**, *5*, 310–317.
26. Eringen, A.C. Simple microfluids. *Int. J. Eng. Sci.* **1964**, *2*, 205–217. [CrossRef]
27. Eringen, A.C. Theory of thermomicrofluids. *J. Math. Anal. Appl.* **1972**, *38*, 480–496. [CrossRef]
28. Ali, V.; Gul, T.; Afridi, S.; Ali, F.; Alharbi, S.O.; Khan, I. Thin film flow of micropolar fluid in a permeable medium. *Coatings* **2019**, *9*, 98. [CrossRef]
29. Khader, M.; Sharma, R.P. Evaluating the unsteady MHD micropolar fluid flow past stretching/shirking sheet with heat source and thermal radiation: Implementing fourth order predictor–corrector FDM. *Math. Comput. Simul.* **2021**, *181*, 333–350. [CrossRef]
30. Kumbinarasaiah, S.; Raghunatha, K. A novel approach on micropolar fluid flow in a porous channel with high mass transfer via wavelet frames. *Nonlinear Eng.* **2021**, *10*, 39–45. [CrossRef]
31. Bhat, A.; Katagi, N.N. Micropolar fluid flow between a non-porous disk and a porous disk with slip: Keller-box solution. *Ain. Shams Eng. J.* **2020**, *11*, 149–159. [CrossRef]
32. Bilal, M.; Saeed, A.; Gul, T.; Kumam, W.; Mukhtar, S.; Kumam, P. Parametric simulation of micropolar fluid with thermal radiation across a porous stretching surface. *Sci. Rep.* **2022**, *12*, 2542. [CrossRef]
33. Abbas, A.; Ahmad, H.; Mumtaz, M.; Ilyas, A.; Hussan, M. MHD dissipative micropolar fluid flow past stretching sheet with heat generation and slip effects. *Waves Random Complex Media* **2022**, 1–15. [CrossRef]
34. Bejawada, S.G.; Nandeppanavar, M.M. Effect of thermal radiation on magnetohydrodynamics heat transfer micropolar fluid flow over a vertical moving porous plate. *Exp. Comput. Multiph. Flow* **2022**, 1–10. [CrossRef]
35. Yadav, P.K.; Verma, A.K. Analysis of two immiscible Newtonian and micropolar fluid flow through an inclined porous channel. *Math. Methods Appl. Sci.* **2022**, *45*, 1700–1724. [CrossRef]
36. Gireesha, B.J.; Anitha, L. Irreversibility analysis of micropolar nanofluid flow using Darcy–Forchheimer rule in an inclined microchannel with multiple slip effects. *Heat Transf.* **2022**. [CrossRef]
37. Alwawi, F.A.; Swalmeh, M.Z.; Qazaq, A.S.; Idris, R. Heat Transmission Reinforcers Induced by MHD Hybrid Nanoparticles for Water/Water-EG Flowing over a Cylinder. *Coatings* **2021**, *11*, 623. [CrossRef]
38. Ibrahim, W.; Zemedu, C. MHD nonlinear mixed convection flow of micropolar nanofluid over nonisothermal sphere. *Math. Probl. Eng.* **2020**, *2020*. [CrossRef]
39. Tabassum, R.; Mehmood, R.; Akbar, N. Magnetite micropolar nanofluid non-aligned MHD flow with mixed convection. *Eur. Phys. J. Plus* **2017**, *132*, 275. [CrossRef]
40. Mkhatshwa, M.; Motsa, S.; Ayano, M.; Sibanda, P. MHD mixed convective nanofluid flow about a vertical slender cylinder using overlapping multi-domain spectral collocation approach. *Case Stud. Therm. Eng.* **2020**, *18*, 100598. [CrossRef]
41. Rahman, M.; Alim, M.; Chowdhury, M. Magnetohydrodynamics Mixed Convection Around a Heat Conducting Horizontal Circular Cylinder in a Rectangular Lid-driven Cavity with Joule Heating. *J. Sci. Res.* **2009**, *1*, 461–472. [CrossRef]
42. Alwawi, F.A.; Alkasasbeh, H.T.; Rashad, A.; Idris, R. Heat transfer analysis of ethylene glycol-based Casson nanofluid around a horizontal circular cylinder with MHD effect. *Proc. Inst. Mech. Eng. C J. Mech. Eng. Sci.* **2020**, *234*, 2569–2580. [CrossRef]
43. Hamarsheh, A.S.; Alwawi, F.A.; Alkasasbeh, H.T.; Rashad, A.M.; Idris, R. Heat transfer improvement in MHD natural convection flow of graphite oxide/carbon nanotubes-methanol based casson nanofluids past a horizontal circular cylinder. *Processes* **2020**, *8*, 1444. [CrossRef]
44. Alwawi, F.A.; Alkasasbeh, H.T.; Rashad, A.; Idris, R. MHD natural convection of Sodium Alginate Casson nanofluid over a solid sphere. *Res. Phys.* **2020**, *16*, 102818. [CrossRef]
45. Dawar, A.; Wakif, A.; Thumma, T.; Shah, N.A. Towards a new MHD non-homogeneous convective nanofluid flow model for simulating a rotating inclined thin layer of sodium alginate-based Iron oxide exposed to incident solar energy. *Int. Commun. Heat Mass Transf.* **2022**, *130*, 105800. [CrossRef]

46. Mansour, M.; Gorla, R.S.R. Mixed convection–radiation interaction in power-law fluids along a nonisothermal wedge embedded in a porous medium. *Transp. Porous Media* **1998**, *30*, 113–124. [CrossRef]
47. Mohammadein, A.; El-Amin, M. Thermal radiation effects on power-law fluids over a horizontal plate embedded in a porous medium. *Int. Commun. Heat Mass Transf.* **2000**, *27*, 1025–1035. [CrossRef]
48. Prasad, V.R.; Vasu, B.; Bég, O.A.; Parshad, R.D. Thermal radiation effects on magnetohydrodynamic free convection heat and mass transfer from a sphere in a variable porosity regime. *Commun. Nonlinear Sci. Numer. Simul.* **2012**, *17*, 654–671. [CrossRef]
49. Gaffar, S.A.; Prasad, V.R.; Reddy, E.K.; Beg, O.A. Thermal radiation and heat generation/absorption effects on viscoelastic double-diffusive convection from an isothermal sphere in porous media. *Ain Shams Eng. J.* **2015**, *6*, 1009–1030. [CrossRef]
50. Alzgool, H.A.; Alkasasbeh, H.T.; Abu-ghurra, S.; Al-houri, Z.; Swalmeh, M.Z. Numerical solution of heat transfer in MHD mixed convection flow micropolar Casson fluid about solid sphere with radiation effect. *Int. J. Eng. Res. Technol.* **2019**, *12*, 519–529.
51. Abbas, A.; Ashraf, M.; Chamkha, A.J. Combined effects of thermal radiation and thermophoretic motion on mixed convection boundary layer flow. *Alex. Eng. J.* **2021**, *60*, 3243–3252. [CrossRef]
52. Patil, P.; Kulkarni, M. Effects of surface roughness and thermal radiation on mixed convective (GO–MoS2/H2O–C2H6O2) hybrid nanofluid flow past a permeable cone. *Indian J. Phys.* **2022**, 1–12. [CrossRef]
53. Abdal, S.; Ali, B.; Younas, S.; Ali, L.; Mariam, A. Thermo-diffusion and multislip effects on MHD mixed convection unsteady flow of micropolar nanofluid over a shrinking/stretching sheet with radiation in the presence of heat source. *Symmetry* **2019**, *12*, 49. [CrossRef]
54. Alkasasbeh, H.T.; Swalmeh, M.Z.; Hussanan, A.; Mamat, M. Effects of mixed convection on methanol and kerosene oil based micropolar nanofluid containing oxide nanoparticles. *CFD Lett.* **2019**, *11*, 55–68.
55. Swalmeh, M.; Alkasasbeh, H.; Hussanan, A.; Mamat, M. Numerical Study of Mixed Convection Heat Transfer in Methanol based Micropolar Nanofluid about a Horizontal Circular Cylinder. *Proc. J. Phys. Conf. Ser.* **2019**, *1366*, 012003. [CrossRef]
56. Ali, A. Unsteady Micropolar Boundary Layer Flow and Convective Heat Transfer. Ph.D. Thesis, Universiti Teknologi Malaysia, Kuala Lumpur, Malaysia, 2010.
57. Kumaran, G.; Sivaraj, R.; Prasad, V.R.; Beg, O.A.; Leung, H.-H.; Kamalov, F. Numerical study of axisymmetric magneto-gyrotactic bioconvection in non-Fourier tangent hyperbolic nano-functional reactive coating flow of a cylindrical body in porous media. *Eur. Phys. J. Plus* **2021**, *136*, 1107. [CrossRef]
58. Howell, J.R.; Mengüç, M.P.; Daun, K.; Siegel, R. *Thermal Radiation Heat Transfer*; CRC Press: Boca Raton, FL, USA, 2020.
59. Swalmeh, M.Z.; Alkasasbeh, H.T.; Hussanan, A.; Mamat, M. Heat transfer flow of Cu-water and Al2O3-water micropolar nanofluids about a solid sphere in the presence of natural convection using Keller-box method. *Res. Phys.* **2018**, *9*, 717–724. [CrossRef]
60. Zeeshan, A.; Majeed, A.; Akram, M.J.; Alzahrani, F. Numerical investigation of MHD radiative heat and mass transfer of nanofluid flow towards a vertical wavy surface with viscous dissipation and Joule heating effects using Keller-box method. *Math. Comput. Simul.* **2021**, *190*, 1080–1109. [CrossRef]
61. Siddiqa, S.; Begum, N.; Hossain, M.A.; Abrar, M.N.; Gorla, R.S.R.; Al-Mdallal, Q. Effect of thermal radiation on conjugate natural convection flow of a micropolar fluid along a vertical surface. *Comput. Math. Appl.* **2021**, *83*, 74–83. [CrossRef]
62. Al-Sawalmeh, M. Numerical analysis of casson ferro-hybrid nanofluid flow over a stretching sheet under constant wall temperature boundary condition. *Front. Heat Mass Transf.* **2022**, *18*. [CrossRef]
63. Nabwey, H.A.; Rashad, A.M.; Khan, W.A. Slip Microrotation Flow of Silver-Sodium Alginate Nanofluid via Mixed Convection in a Porous Medium. *Mathematics* **2021**, *9*, 3232. [CrossRef]
64. Singh, K.; Pandey, A.K.; Kumar, M. Numerical solution of micropolar fluid flow via stretchable surface with chemical reaction and melting heat transfer using Keller-Box method. *Propuls. Power Res.* **2021**, *10*, 194–207. [CrossRef]
65. Swalmeh, M.Z.; Alkasasbeh, H.T.; Hussanan, A.; Nguyen Thoi, T.; Mamat, M. Microstructure and inertial effects on natural convection micropolar nanofluid flow about a solid sphere. *Int. J. Ambient Energy* **2022**, *43*, 666–677. [CrossRef]
66. Rafique, K.; Alotaibi, H. Numerical Simulation of Williamson Nanofluid Flow over an Inclined Surface: Keller Box Analysis. *Appl. Sci.* **2021**, *11*, 11523. [CrossRef]
67. Cebeci, T.; Bradshaw, P. *Physical and Computational Aspects of Convective Heat Transfer*; Springer Science & Business Media: Berlin/Heidelberg, Germany, 2012.
68. Nazar, R.; Amin, N.; Pop, I. Mixed convection boundary layer flow about an isothermal sphere in a micropolar fluid. *Int. J. Therm. Sci.* **2003**, *42*, 283–293. [CrossRef]
69. Alwawi, F.A.; Hamarsheh, A.S.; Alkasasbeh, H.T.; Idris, R. Mixed Convection Flow of Magnetized Casson Nanofluid over a Cylindrical Surface. *Coatings* **2022**, *12*, 296. [CrossRef]